Experimental and Numerical Analysis of Microstructure and High-Temperature Tensile Behavior of a Directionally Solidified Superalloy

M. Torfeh, S.M.H. Mirbagheri, S. Nakhodchi, and J. Aghazadeh Mohandesi

A comprehensive cellular automaton algorithm coupled with finite element method was developed for the simulation of temperature field, heat transfer characteristics and the anisotropic grain growth during a directional solidification (DS) process. Nucleation parameters at the interface of the alloy and the chill plate were adjusted at four levels, and the evolution of macrostructure during competitive growth of grains has been characterized. The sensitivity of grain structure to heat transfer coefficients between alloy/chill plate and alloy/ceramic mold was also evaluated at a constant nucleation condition. The results were compared with the microscopic images and measurements of the experimentally cast DS specimens. This model was then utilized for the development of another micro-mechanical finite element model of the cast bars including the realistic grain boundaries and misorientations. To complete a simulation of a whole manufacturing chain from casting process to mechanical behavior evaluation, high-temperature tensile behavior of the cast bars was then elucidated through experiment and FE analysis.

1. Introduction

In general, the efficiency of the land-based gas turbines or aero-engines is significantly affected by their firing temperature. Therefore, the development of functional materials at higher temperatures is one of the routes for further improvement in turbine performance. Hence, the researches were conducted on the high-temperature materials developments, as well as the technology used for manufacturing the directionally solidified (DS) and single-crystal (SC) materials (Ref 1). For instance, in the DS casting process, a columnar-grained structure with the grain boundaries lined up in a predesigned direction is desired. Therefore, a unidirectional heat transfer has to be generated to push the solid/liquid interface only in one direction (Ref 2). Ideally, growth direction of dendrites in FCC alloys is (100) direction; hence, any misorientation with respect to the heat transfer direction will lower the growth rate (Ref 3). Furthermore, the mold temperature is required to remain considerably higher than the liquidus temperature, so a proper vertical thermal gradient is achieved that will prevent distinct nucleation in front of the liquid–solid interface or at the mold surface (Ref 4). The final DS product has normally substantially enhanced mechanical properties such as high-temperature creep (Ref 5-7), fatigue (Ref 8) and corrosion (Ref 9). However, these advantages may not be similar in all alloys (Ref 10). In the Bridgman process (Ref 11), which is the most common method of DS casting, a preheated ceramic shell mold is filled with molten alloy in a dual-zone furnace. Then, the mold–alloy set is driven from the hot zone at a predefined velocity to a second area of the furnace where the radiational heat transfer enforced for cooling of the melt (Ref 2).

The GTD111 is one of the Ni-based superalloys that have been manufactured in both forms of equiaxed (EA) and directionally solidified (DS). The polycrystalline GTD111 was first developed by General Electric (GE) in the 1970s as the first stage rotary blades of a land-based gas turbine. Due to improvement in its material properties, the alloy was suggested for substitution of the commercial IN738LC superalloy for the turbines with higher combustion temperatures (Ref 12). The DS-GTD111 was later developed and it was widely used in land-based gas turbines such as the first stage blade in MS7F/MS9F, MS3002 and MS5002C gas turbines (Ref 12).

Finite element analysis is a beneficial technique used to reduce the number of experiments and prototypes. It is also employed for obtaining an in-depth knowledge of complicated processes such as casting (Ref 13-16). The cellular automaton (CA) approach (Ref 13, 17, 18) is one of the probabilistic methods, in which all intended physical rules are used to determine the state of each cell in relation to the state of neighboring cells. In this method, the state of all cells is calculated simultaneously which results in more efficiency. A CA-based solidification model developed by Gandin and Rappaz has determined relation between dendrite growth and orientation with local undercooling (Ref 17) which was shown to predict well dendritic structures formation in Bridgeman furnace cooling condition (Ref 19). Heterogeneous nucleation sites are assumed to have a Gaussian distribution (Ref 14). Accordingly, a numerical solidification analysis was conducted through a cellular automaton and finite elements combined method (Ref 20, 21). The modeling of the solidification process can lead to a prediction of the thermal and flow profiles. These

M. Torfeh, S.M.H. Mirbagheri, and **J. Aghazadeh Mohandesi,** Department of Materials and Metallurgical Engineering, Amirkabir University of Technology, Tehran, Iran; and **S. Nakhodchi,** Mechanical Engineering Department, K.N. Toosi University of Technology, Tehran, Iran. Contact e-mail: smhmirbagheri@aut.ac.ir.

models provide a ground for the study of dendrite nucleation, morphology and growth rate. Furthermore, the calculation of primary dendrite arm spacing (PDAS) and secondary dendrite arm spacing (SDAS) which have a significant influence on the mechanical properties of directionally solidified superalloys, can be facilitated (Ref 21-24). Near to real microstructures obtained through this method can provide the opportunity to have a 3D model of components and their grain structures simultaneously. Thus, further numerical evaluation of grain structure effect on such components in mechanical behavior modeling and life prediction rules can be simply carried out.

In the present study, the evolution of columnar grain formation during directional solidification of GTD111 superalloy is explored both experimentally and numerically. The grain nucleation parameter's effects on the predicted grain structure and SDAS are evaluated numerically and compared to real specimens. Then the resulted microstructures are applied for high-temperature tensile test simulation, in order to find a tool for mechanical behavior prediction of any grain geometry and misorientation distribution.

2. Experimental Procedure

2.1 Casting Process

The material used in the casting process was GTD-111DS Ni-based superalloy which has a chemical composition close to Rene80 and IN738LC superalloy (Ref 25, 26). Using Oxford optical emission spectroscopy (OES), the chemical composition of the superalloy primary ingots was defined and is presented in Table 1.

Vacuum induction melting (VIM) furnace (10^{-3} mbar) was used for the casting process. Figure 1(a) and (b) presents the wax model of the casting and riser assembly and the alumina shell mold placed on a water-circulating copper plate applied to produce a set of directionally solidified bars in a circular arrangement. The manufacturing process produced 16 bars of 12 mm diameter and 190 mm length. Molten alloy pouring was carried out at 1500 °C, and then, the casting was drawn downward at a rate of 4 mm/min to conduct the growth of the grains in the axial direction.

2.2 Metallurgical Investigation

Metallurgical investigations were carried out on the final casting bars at the surface and the transversal and longitudinal sections. A macro-etch reagent of $FeCl_3$ + HCl was applied to display the surface grain structure of the cylindrical casting bars. A similar reagent was used on longitudinal sections of rods, which was followed by stereo-microscopy to reach a better contrast on surface grain pictures.

Microstructural analysis of the bars was performed using an Olympus optical microscope at multiple cross sections. Each section was sequentially polished using silicon carbide paper of grit size ranging from 120 to 2500. Final polishing was carried out using alumina suspension with 1 μm particle size. The specimens were then etched in two stages using Waterless Kalling's (5 g $CuCl_2$ + 100 mL HCl + 100 mL ethyl alcohol) and Adler etchants (9 g Cl_3CuH_4N + 150 mL HCl + 45 g $FeCl_3$ + hydrated DI water), respectively.

2.3 High-Temperature Tensile Testing

Three tensile specimens were cut and machined from the upper one-third of the cast bars where the grains are mostly aligned with the longitudinal axis (Fig. 2). Thus, the misorientation of the grains was expected to be the minimum. Then, tensile tests were conducted at 650 °C according to the ASTM E8M standard (Ref 27) using a SATEC servohydraulic testing machine. The fracture surfaces and microstructure of tensile specimens were studied using field emission scanning electron microscopy (FE-SEM).

3. FE Microstructure Modeling

Several parameters in directional solidification, e.g., the furnace specifications, alloy chemical composition, heat extraction parameters and nucleation parameters, have been reported to be influential on final microstructure. Among these, nucleation parameters and heat transfer coefficients were chosen to be studied due to their remarkable effect on the number of nucleated crystals and orientations of directionally solidified grains. Furthermore, the main focus in the directional solidification is the control over the grain boundaries in a way that promote the growth of dendrites along the longitudinal direction. Certainly, the optimum properties are attained when the proper volume fraction of γ' phase and carbide precipitates are formed during heat treatment. Since considering all macroscopic and microscopic parameters in the simulation is not possible, microstructural anomalies and inhomogeneities such as γ' size variations (between the dendrite core and the interdendritic zone), and the effects of the carbides and detrimental TCP precipitates were neglected in the evaluation of the effects of the grain boundaries and misorientations.

3.1 Solidification Modeling

The domain adopted for the casting process simulation is shown in Fig. 3. It was a one-eighth section of the total casting cluster consists of two test bars out of sixteen as well as the equivalent section of the furnace and alumina mold. During the directional casting process, the heat was mainly transferred through the radiation from the heating elements of the furnace and it was then conducted through the furnace lining and the mold. Therefore, the simulation was simplified by neglecting the effect of filling stages. A similar approach was reported previously (Ref 15). Hence, the mold was instantaneously filled with 1500 °C molten alloy such that all bars were in contact

Table 1 Chemical composition of GTD-111DS (wt.%)

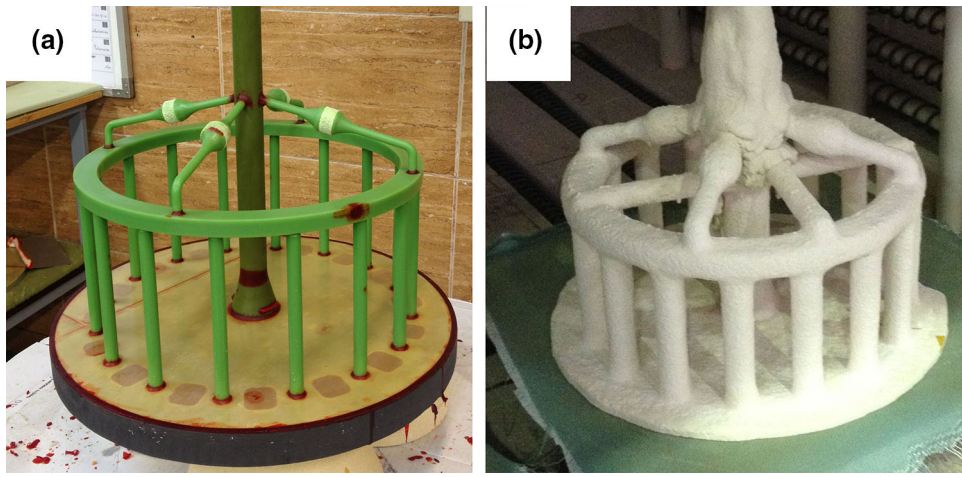| Element	C	Cr	Co	W	Mo	Ti	Al	Ta	Ni
wt.%	0.08	13.44	9.50	4.18	1.80	4.71	3.07	2.62	Bal.

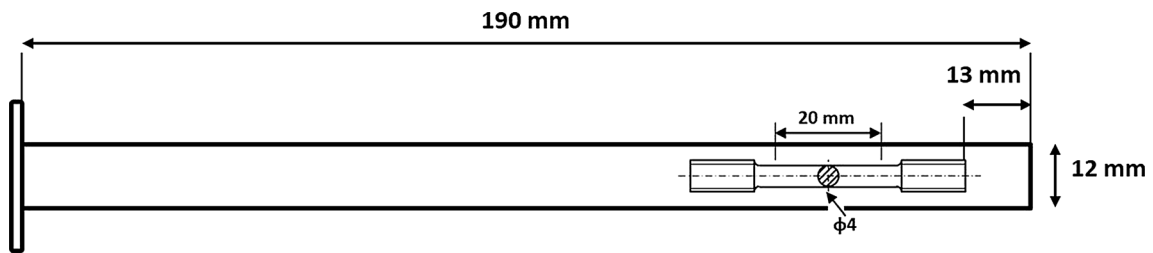**Fig. 1** Casting process details: (a) wax assembly and (b) and ceramic shell mold

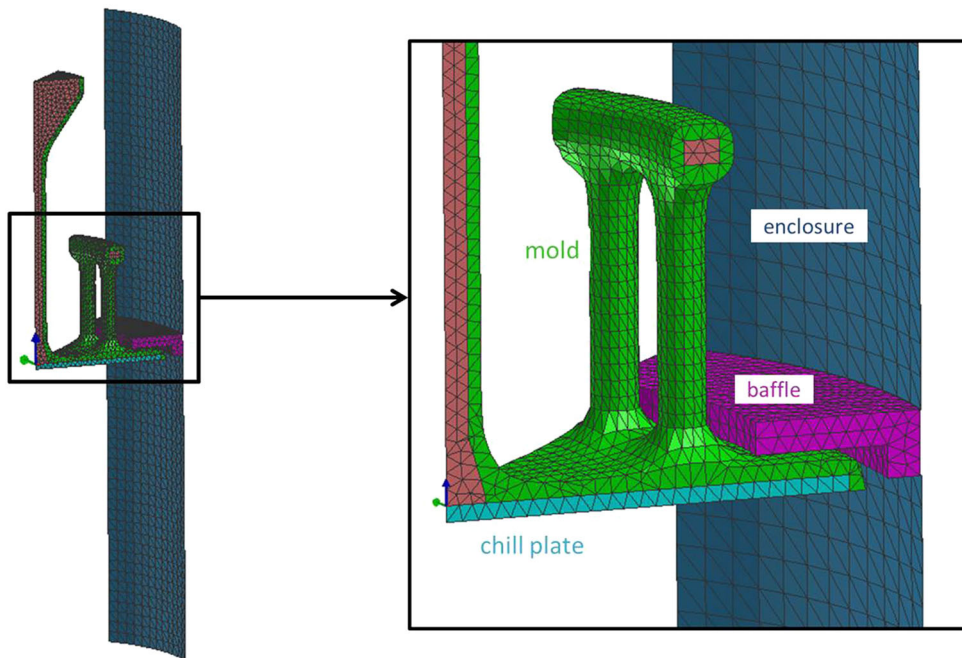**Fig. 2** Tensile specimen schematic and its position in casting bar

Fig. 3 Finite elements mesh of one-eighth of casting cluster in addition to chill plate, thermal baffle, shell mold and peripheral thermal insulation

with a 15 °C chill plate. The back wall of the furnace was introduced as an enclosure to control the heat transfer through the radiation. The solidification process was conducted by moving the castings and the chill plate downward with a constant velocity of 4 mm/min. The subsequent grain nuclei were grown in the direction of the test bars axis.

The solidification progress was simulated using a 3D cellular automaton approach model (Ref 20). The nucleation

equation for the grain formation modeling (Ref 14, 28) was taken into account as:

$$\frac{dn}{d(\Delta T)} = \frac{n_{max}}{\sqrt{2\pi}\Delta T_\sigma} \exp\left[-\frac{(\Delta T - \Delta T_m)^2}{2\Delta T_\sigma^2}\right] \quad \text{(Eq 1)}$$

where ΔT is the undercooling (°C), n_{max} is the maximum number of nuclei per unit area, and ΔT_m and ΔT_σ are the mean undercooling (°C) and the standard deviation (°C) of the Gaussian nucleation distribution, respectively. Four sets of nucleation conditions were used to define the related microstructural effects. The nucleation conditions designated by state codes A, B, C and D had various ΔT_m, ΔT_σ and n_{max} that are presented in Table 2. The dendritic grain growth rate (V_{tip}) was applied according to Kurz, Giovanola and Trivedi (KGT) model (Ref 29):

$$V_{tip} = \alpha(\Delta T)^2 + \beta(\Delta T)^3 \quad \text{(Eq 2)}$$

where ΔT is the undercooling (°C), while α and β are the surface and volume growth coefficients, respectively. The grain growth coefficients α and β of KGT model were calculated as $\alpha = 7.29097E{-}8$ m/s/K^2 and $\beta = 9.66761E{-}9$ m/s/K^3 for GTD111DS alloy using ProCAST software.

For conditions codes of A, B, C and D which had various nucleation parameters, the heat transfer coefficient of 100 W/m^2 K was considered at the contact surfaces of alloy/mold along with the heat transfer coefficient of 1000 W/m^2 K at the alloy/chill interface. Three other heat transfer conditions named as state codes E, F and G with similar nucleation parameters as state code A were introduced, as listed in Table 2, to gain insight into the effects of various heat transfer coefficients during the casting process. Similar to the experimental process, as the castings and the chill plate were moved downward by a constant velocity of 4 mm/min, solidification of the superalloy went forward and the nucleated grains grew along the bar longitudinal axis.

Bulk nucleation during the directional solidification was assumed to be negligible; thus, grain nucleation occurred only at alloy–chill interface.

3.2 High-Temperature Tensile Modeling

Finite element simulations were performed to predict the high-temperature tensile behavior of the GTD111DS alloy considering the grain boundaries and misorientations. The FE domain included the full geometry of the gauge size of a tensile test specimen that is built based on the predicted grain structure obtained in the solidification model. The location of test specimen in the simulated bar was identical to the location of real specimen in the cast bar. The purpose of such modeling was introducing a new procedure to obtain a geometrical model of the microstructure, instead of classical multiple sectioning

Table 3 Anisotropic elastic and Hill's parameters of GTD111DS at 650 °C (Ref 49)

Elastic parameters		Hill's parameters	
E_1, E_2, GPa	156.2	F, –	0.32
E_3, GPa	120.9	G, –	0.32
v_{13}, v_{31}, –	0.195	H, –	0.25
v_{12}, –	0.4	L, –	1.05
G, MPa	97.9	M, –	1.05
		N, –	0.81
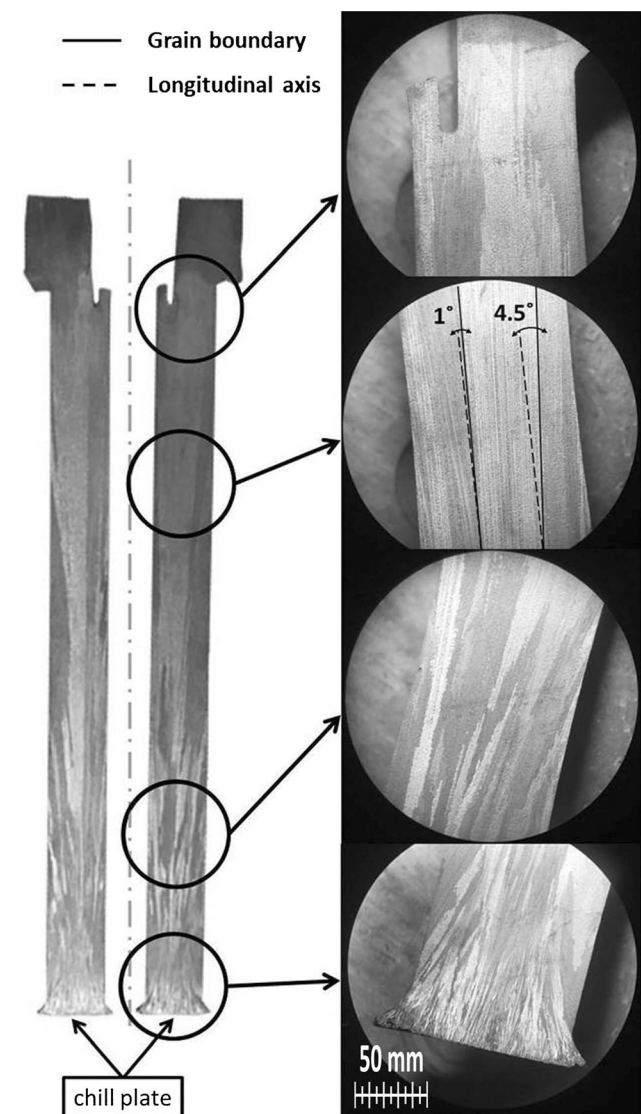
Fig. 4 Grain structure at longitudinal section of a real cast specimen

Table 2 Simulation conditions for modeling directional solidification

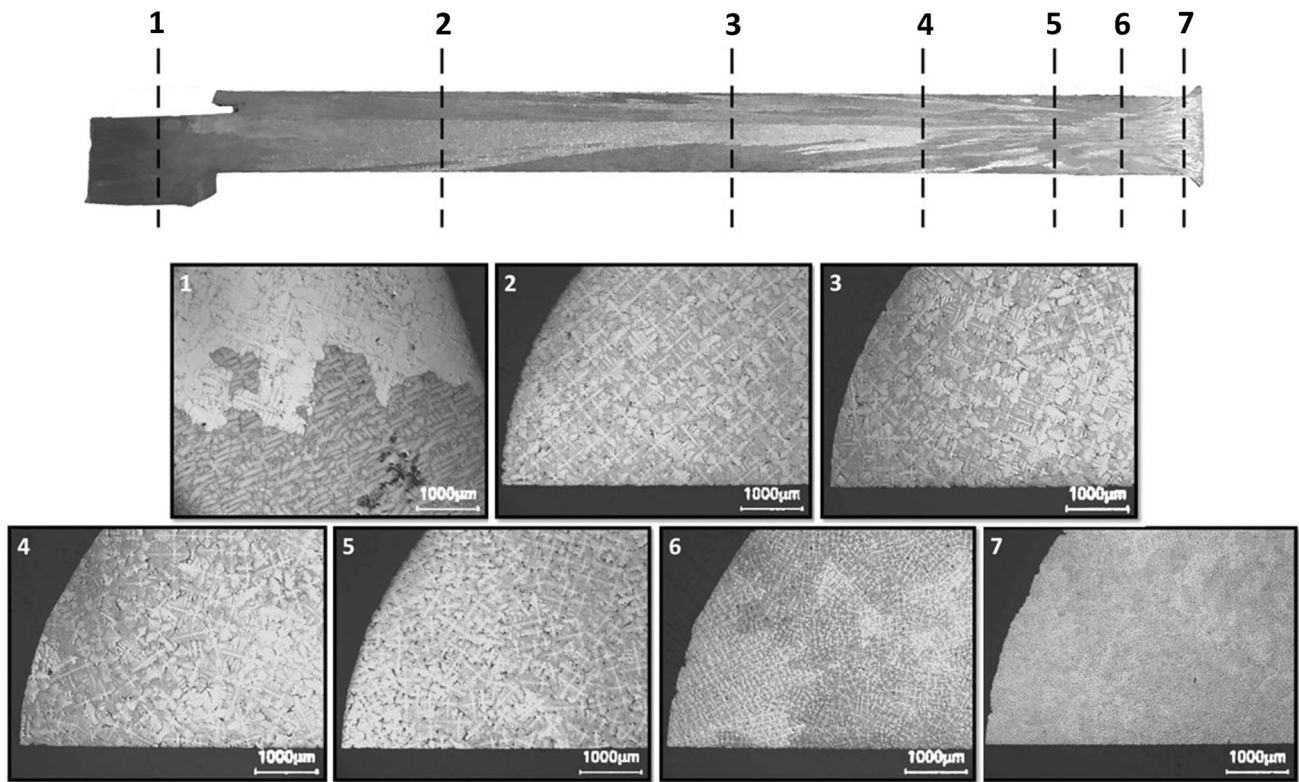| State code	ΔT_m, °C	ΔT_σ, °C	n_{max}, m^{-2}	$H_{alloy/chill}$, W/m^2 K	$H_{alloy/mold}$, W/m^2 K
A	10	1	10^6	1000	100
B	5	1	10^8	1000	100
C	10	1	10^8	1000	100
D	0.5 (Ref 16)	0.3 (Ref 16)	10^7 (Ref 16)	1000	100
E	10	1	10^6	2000	100
F	10	1	10^6	2000	500
G	10	1	10^6	1000	500

Fig. 5 Evolution of dendritic microstructure at cross sections of a real cast specimen

methods. The predicted geometry of the solidified bar was imported from the solidification model explained in the above section; hence, the grain geometries and orientations were also imported. The FE mesh is presented later in section 6-5, for which class C3D8R linear brick elements were used. Each grain was assumed to be transversely isotropic, which means isotropy was only defined in X–Y plane, i.e., $E_1 = E_2 = E_T$, $v_{12} = v_{21}$, $v_{13} = v_{23}$, $v_{31} = v_{32}$, $(v_{31}/E_3) = (v_{13}/E_1)$ and $G_{13} = G_{23}$. Equation 3 (Ref 30) describes the grain elastic behavior. The anisotropic elastic properties of GTD111DS at 650 °C (Ref 31) presented in Table 3 were used for predicting elastic behavior. The simulation was performed using ABA-QUS software code.

$$\begin{bmatrix} \varepsilon_{11} \\ \varepsilon_{22} \\ \varepsilon_{33} \\ \varepsilon_{12} \\ \varepsilon_{23} \\ \varepsilon_{13} \end{bmatrix} = \begin{bmatrix} \frac{1}{E_1} & -\frac{v_{12}}{E_1} & -\frac{v_{31}}{E_3} & 0 & 0 & 0 \\ -\frac{v_{12}}{E_1} & \frac{1}{E_1} & -\frac{v_{31}}{E_3} & 0 & 0 & 0 \\ -\frac{v_{13}}{E_1} & -\frac{v_{13}}{E_1} & \frac{1}{E_3} & 0 & 0 & 0 \\ 0 & 0 & 0 & \frac{1}{2G_{13}} & 0 & 0 \\ 0 & 0 & 0 & 0 & \frac{1}{2G_{13}} & 0 \\ 0 & 0 & 0 & 0 & 0 & \frac{1+v_{12}}{E_1} \end{bmatrix} \begin{bmatrix} \sigma_{11} \\ \sigma_{22} \\ \sigma_{33} \\ \sigma_{12} \\ \sigma_{23} \\ \sigma_{13} \end{bmatrix}$$
(Eq 3)

Hill's anisotropic equivalent stress (Eq 4) was chosen for the calculation of the specimen plastic deformation by calculating the Hill's constants of F, G, H, L, M and N for GTD111DS bars (Table 3), as defined in the literature (Ref 32, 33).

$$\sigma_{eq} = \sqrt{F(\sigma_{22}-\sigma_{33})^2 + G(\sigma_{33}-\sigma_{11})^2 + H(\sigma_{11}-\sigma_{22})^2 + 2L\sigma_{23}^2 + 2M\sigma_{31}^2 + 2N\sigma_{12}^2}$$
(Eq 4)

4. Results and Discussion

4.1 Metallurgical Investigation

Figure 4 illustrates the macro-etched longitudinal section of a cast bar specimen. The trend of annihilating high-angle boundaries by getting away from the chill plate is evident in Fig. 4. Numerous grains were nucleated at the interface of the superalloy and the chill plate with arbitrary orientations which most of them were converging toward the core of the bar. Rosenberg et al. (Ref 34) showed that the preferred orientation of primary dendrites in FCC structured alloys is ⟨100⟩ direction. Thus, adjusting the heat flow direction at the predefined axis of the casting results in the growth of the dendrites at a preferred direction. However, perturbations that may occur in the solidification front mostly make it challenging to reach such ideal orientation (Ref 35). Macrostructure of the bar near the chill plate (Fig. 4) shows deviation angle of more than 30°. At the upperparts, highly misoriented grains were eliminated; thus, the maximum detected deviation of dendrites was 4.5°.

The dendritic microstructure evolution on the cross sections of the bar is also shown at different heights in Fig. 5. The dendritic microstructure and secondary dendrite arms are displayed in seven cross section. An enormous number of grains were recognized at the cross section adjacent to the chill plate. Getting far from the chill plate, the number of grains was constantly decreasing, while dendrite secondary arms had increased in size.

4.2 Numerical Modeling

The latent heat released during the solidification process was considered in calculations due to its influences on the cooling
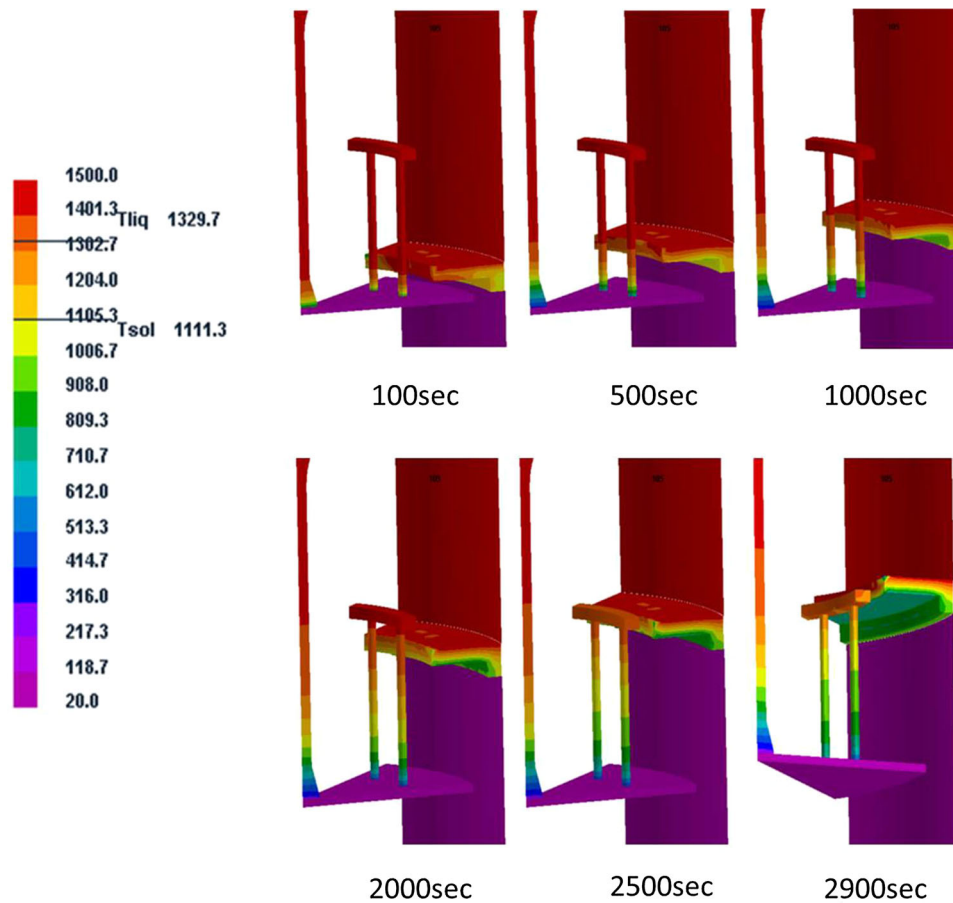
Fig. 6 Temperature distribution predictions in the melt, baffle and riser during the directional solidification

rate. Hence, the temperature distribution of the furnace chambers, shell mold and casting during the process was predicted.

Figure 6 illustrates the temperature distribution prediction in the different parts of the casting system including bars, riser and baffle during the transient solidification process. The temperature at chill plate and enclosures had been kept constant. In such configuration, upper enclosure and baffle compensate the lateral heat transfer of bars through radiation. As the castings were drawn downward, the fraction of the cluster that were entered to the lower and cooler chamber started to solidify. The mushy zone, which is defined by liquidus and solidus isothermal surfaces, had been kept in front of the baffle to provide a planar solidification front (Fig. 7).

The prediction of the temperature history at the 12 locations along the bars is compared in Fig. 8. The central axis of one of the casting bars in the FE mold was divided by 12 points with an approximate distance of 20 mm from each other (Fig. 8(a)), and the temperature records of these points are compared in Fig. 8(b). The cooling rates shown in Fig. 8(a) are decreased as the longitudinal distance from the chill plate is increased. Controlling lateral heat flow in DS process is critical (Ref 36) as the lateral heat flow declines by increasing the thermal conductivity ratio between the alloy and ceramic mold (Ref 37). Therefore, five points were selected at the transversal section of the mid-height of the bar and the temperature variations at radial and peripheral directions are shown in Fig. 8(c) and (d). Comparing the cooling rate at the cross section of mid-height of

bars revealed negligible deviation in both radial and peripheral directions (Fig. 8(d)). This result was predictable due to the geometry and small diameter of cylindrical bars; however, it can be greatly different for complicated components, e.g., turbine blades (Ref 37). Hence, further evaluations were performed only at the longitudinal direction of the bars. The built-up of internal stresses during directional solidification due to different thermal gradients in each direction has been discussed elsewhere (Ref 38).

The predicted temperatures were employed for the determination of the liquid alloy undercooling to determine the grain growth kinetics. Hence, the final grain structures at two heights of the specimens are compared with the experiments in Fig. 9. To have a more precise evaluation of the casting parameters effects on the microstructure, SDAS had been chosen as a quantitative factor (Ref 39). SDAS was calculated through Eq 5, where t_s was solidification time at a point and M and n were alloy constants.

$$\lambda_2 = (M \cdot t_s)^n \qquad (Eq\ 5)$$

4.3 Nucleation Parameters Effect

Based on Eq 1, the microstructure of the solidified specimen is controlled by three variables. There is a Gaussian distribution for heterogeneous nucleus density (Ref 40). By increasing the maximum active nucleation sites, the final microstructure is more dominated by the nucleation process, and hence, finer grain size can be achieved. This effect is shown in Fig. 9 in
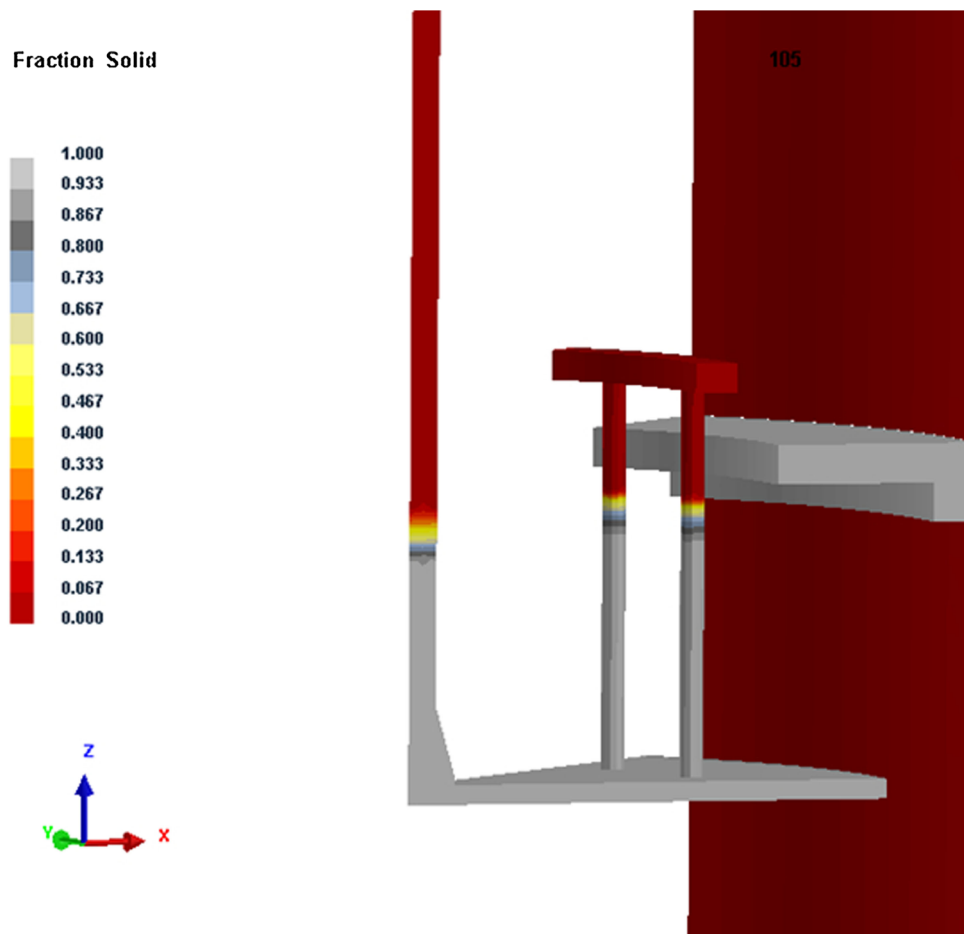
Fig. 7 Mushy zone position in relation to baffle during the directional solidification

which the resulted microstructure for four different sets of parameters that are defined in Table 2 has been shown at two different heights. The polished and etched cross section of the real specimen at the same heights of 2 and 100 mm distance from the chill plate has also been included for microstructural comparison. Figure 9 shows that *B* and *C* states lead to a greater number of grains and finer grain structure at both heights. It is evident that the grain structure is more sensitive to the maximum density of the nuclei and less dependent on the ΔT_m. This can be attributed to the fact that states *B* and *C* were defined with the same nucleus density having a 50% difference in the ΔT_m; however, the microstructure and the resulted grain density are similar. It is worth noting that the growth variables have been kept constant for all four states. Figure 10(a) and (b) shows the variation of the grain density and misorientation from $\langle 001 \rangle$ direction along the bar, respectively. It is evident that the states *B* and *C* are following the same trend in both figures. Also, the grain density seems to be more dependent on nucleus density than undercooling. The nucleus density of state *A* is two orders of magnitude greater than states *B* and *C*, and state *D* is the middle condition; the undercooling of states *A* and *C* are two times greater than of state *B*. In other words, while

the maximum undercooling is the same between *A* and *C*, and differs from *B*, the resulting grain densities of *B* and *C* are much closer to each other than that of *A*.

Figure 9 and 10 demonstrates the dependency of the grain structure on the nucleation parameters and the distance from the chill plate. The simulation results of all four sets of parameters show a monotonic decreasing curve with a sharp drop in both grain density and misorientation, in the vicinity of the chill plate. As the grain nucleation was assumed to be limited to the interface of the alloy and the chill plate, the solidification process in other regions of the specimen was more dominated by the grain growth rather than the grain nucleation. The sharp temperature drop in the regions adjacent to the chill plate (Fig. 8) resulted in an instantaneous nucleation (Ref 28) and generation of a thin layer of fine grain structure. As the solidification front migrates further from the chill, the impact of longitudinal temperature gradient diminishes. This leads to the elimination of the initially formed grains and thus a lower grain density. Figure 9 shows that the difference in the microstructure and grain size is much more pronounced in section 1 than section 2, which proves that the effect of the nucleation parameters decreases by moving away from the chill plate.
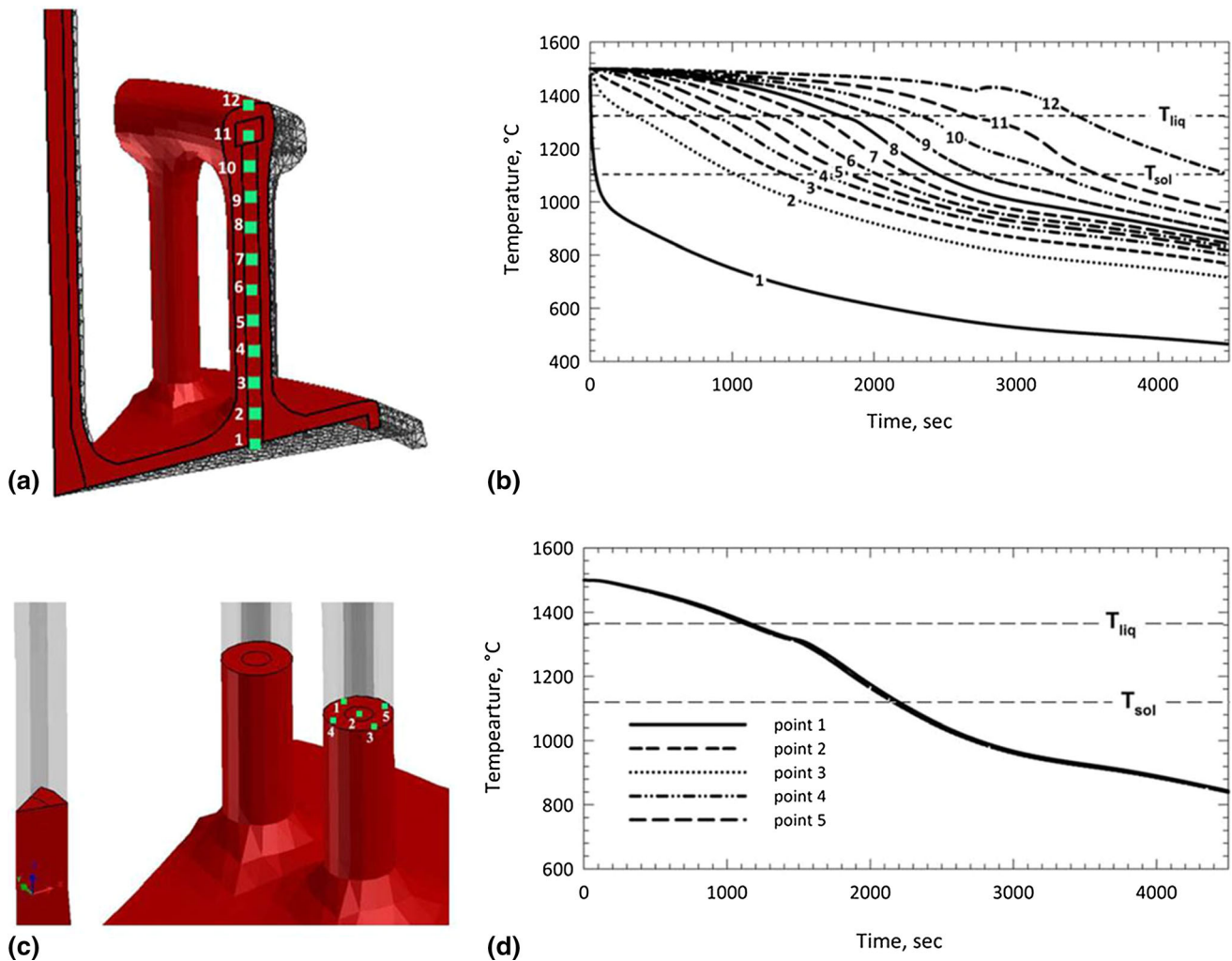
Fig. 8 Temperature history at different points in (a, b) longitudinal section and (c, d) cross section of a bar

Toward the end of the solidification, the slop of the diagram in Fig. 10 decreases and the microstructural change is negligible and less dependent on the nucleation variables.

Figure 11 shows the solidification time versus distance from the chill plate for all four sets of parameters. The negligible difference between the sets shows that there is no relation between the nucleation parameters and solidification time and it is strictly growth dependent. Based on Eq 4, it could also be deduced that these parameters have no noticeable impact on the SDAS. In general, the dendritic growth direction and distance are a function of the alloy composition, temperature gradient and solidification rate which control the stability of the dendrite tip in the solidification front (Ref 41, 42).

4.4 Interfacial Heat Transfer Coefficient Effect

The initial simulation was performed based on the heat transfer coefficients presented as state code *A* in Table 2 that was reported in Ref 20 and 43. It should be noted that several parameters may practically alter the interface heat transfer coefficients such as interface roughness, application of pressure, interface orientation regarding gravity and melt surface tension (Ref 44, 45). Therefore, further analyses were carried

out as state codes *E*, *F* and *G* in Table 2. It should be noted that nucleation parameters in such four states remained similar. The microstructural predictions at the same location as Fig. 9 are shown in Fig. 12 where effects of interface heat transfer coefficients can be seen for mentioned state codes. The temperature gradients were also calculated at each node along the longitudinal axis of cast bars. The results are then compared in Fig. 13 showing the effects of heat transfer coefficients at the interfaces. It can be seen that states *G* and *F* have the upper and lower limits, respectively. It can also be seen that at the heights upper than 120 mm from the chill plate, effects of heat transfer coefficients can be neglected and all four curves have an identical trend.

Figure 14 shows solidification time along the longitudinal axis of modeled cast bars in four thermal states. At the first 50 mm from the chill plate, bars with $H_{alloy/mold}$ of 100 W/ m^2 K had experienced lower solidification times, states *A* and *E*. The trend appeared to be going in the reverse direction at the upper sections. Therefore, the increase in $H_{alloy/mold}$ to 500 W/ m^2 K in states *F* and *G* resulted in a drop in solidification time. As a result, the change of $H_{alloy/mold}$ had a much considerable effect on solidification time and also on SDAS, according to Eq 4.
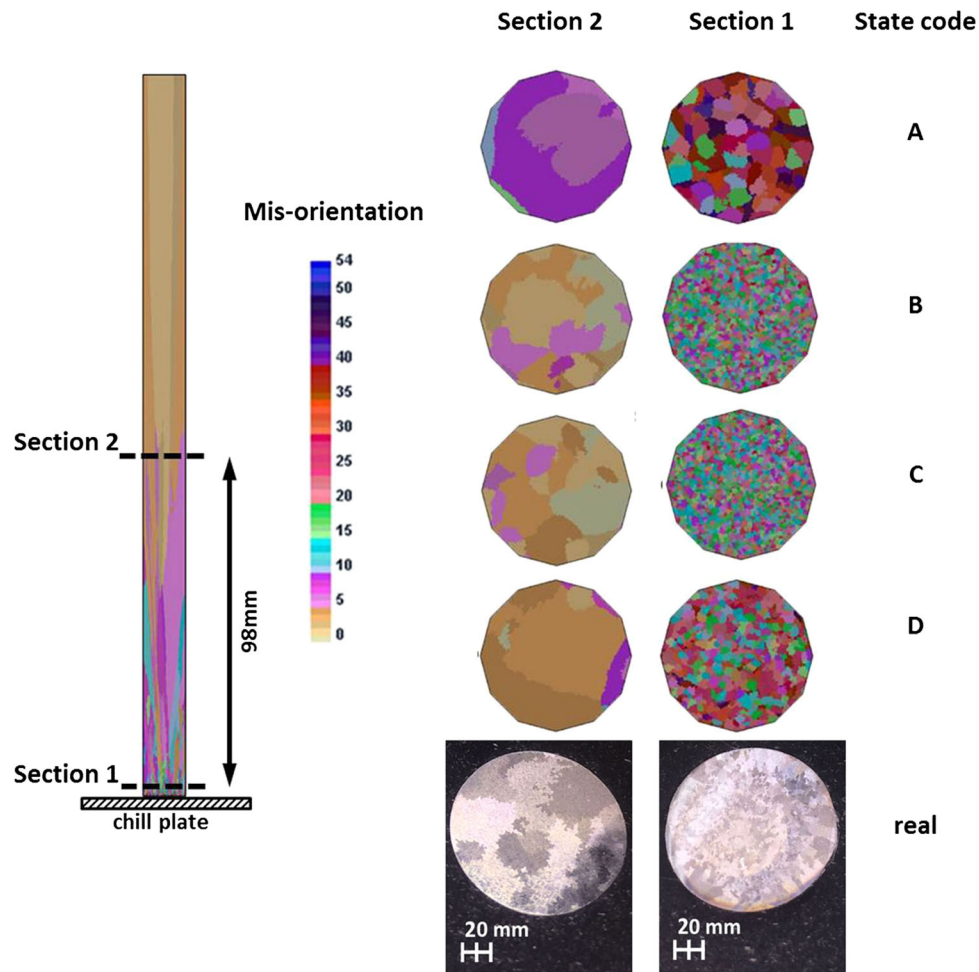
Fig. 9 Effect of nucleation parameters on microstructure at two heights of 2 and 100 mm

The longitudinal section of the real directionally solidified specimens is shown in Fig. 15 which reveals the unidirectional growth of the dendrites. Secondary dendrite arm spacing was also measured in the real specimens along the bars longitudinal axis. Considering the scatter band of solidification time (Fig. 14) and the measured SDAS, the unknown coefficients of $n = 0.48$ and $17 < M < 20$ were achieved for Eq 4.

The thermal gradient and cooling rate are the two important parameters controlling microstructure and grain structure of solidified alloys. Generally, reaching single crystals and directionally columnar-grained structures needs high thermal gradient and very low cooling rates. Ideally, the thermal gradient should be increased at very low cooling rates to change the directionally columnar-grained structures into single-crystal structure. However, it is difficult to set such a configuration. Figure 13 reveals that the thermal gradient in all four heat transfer states had limited to a narrow range of 3.0-4.8 K/mm at upper sections of the bars. Considering that the growth rate had been remained at a constant amount of 4 mm/s due to controlled progress of solidification front in Bridgeman furnace, a cooling rate of 12-19 K/s had been experienced.

4.5 High-Temperature Tensile Behavior Experiment and Simulation

Three high-temperature tensile test results showed average yield stress of 819 MPa that is consistent with the literature (Ref 46). The average ultimate tensile stress of 1200 MPa and the average elongation of 16% were also achieved which is higher than 7-10%, the reported amount for longitudinal direction at 650 °C (Ref 13, 46, 47). It should be noted that the GTD111DS superalloy exhibits a remarkable increase in the yield stress, UTS and elongation in the range of 600-800 °C in the longitudinal direction due to change in the slip system of γ' phase from octahedral to cubic (Ref 5, 48-50). The microstructure of cross section of the specimen, below fracture surface, is presented in Fig. 16. The microstructure comprised of typical Ni-based superalloys components, i.e., duplex γ' precipitates, MC carbides rich in Ta, Ti and W, and $\gamma-\gamma'$ eutectics. As depicted in Fig. 17, the observations of the specimen fracture surfaces revealed a fracture surface normal to the loading direction, with some small inclined areas. This can be associated with multiple grains in cross section of a DS material fracture at different angles, leading to an uneven transgranular fracture surface. The same behavior was reported by other researchers (Ref 39, 48, 50). The SEM images (Fig. 17(b) and (c)) also show cleavage facets at both edge and core of the fracture surface. These observations along with low reduction area of fracture surface led to the conclusion that the alloy had a brittle fracture. A similar behavior has been reported for directionally solidified superalloys at intermediate temperatures (Ref 47, 51, 52).

Finite element simulations were performed to predict the high-temperature tensile behavior of the GTD111DS consider-
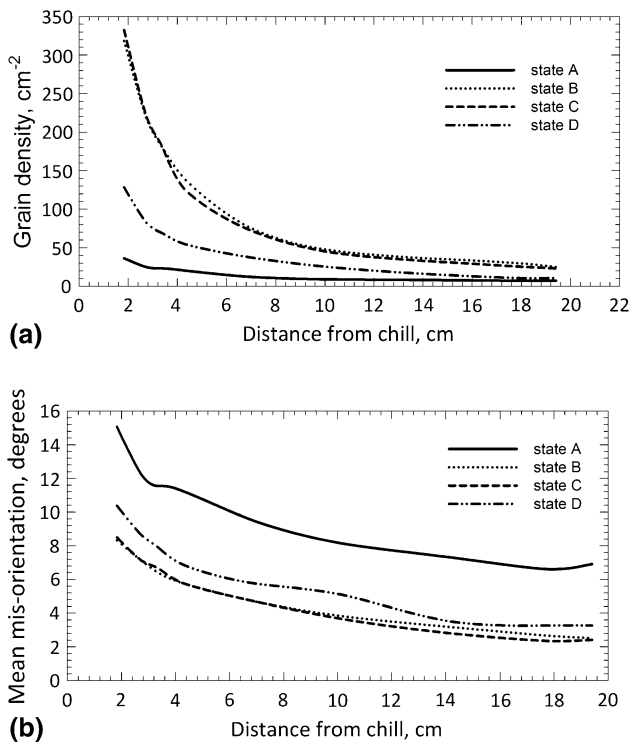
Fig. 10 Effect of nucleation on (a) cross-sectional grain density and (b) mean misorientation

Fig. 11 Effect of nucleation parameters on solidification time

ing the predicted misorientation of the grains to provide a simulation of the whole manufacturing chain from casting process to mechanical properties evaluation. Grain geometries and misorientation at mid-height cross section of state *C* modeled specimen, as the closest structure to real bars in Fig. 9, were extracted and used for 3D model construction. It should be noted that all longitudinal grain boundaries were assumed to be parallel to *Z* axis to simplify the 3D model (Fig. 18). The Euler angles of each grain were assigned to the FE model by introducing a local coordination, and the grains were tied to each other. The anisotropic elastic and plastic properties presented in Table 3 were used for predicting tensile behavior.

Figure 19(a) illustrates the average stress–strain curve were extracted from all nodes of grains at the necking. It is also compared to the experimentally obtained results that revealed an acceptable fit. The significance of introducing grains in the model is clearly displayed in Fig. 19(b). The solid line in Fig. 19(b) shows the stress–strain curve of an element at the necking of a simple cylindrical specimen with a 4° deviation from *Z* axis and no grain boundaries. Although the highest misorientation of the first model was applied, the tensile behavior of the specimen had changed by removing grain boundaries showing less strain hardening.
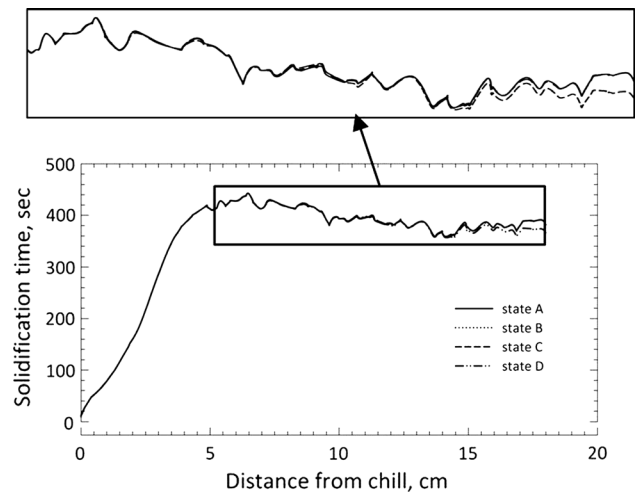
On the other hand, any variation of grain Euler angles with similar grain geometries resulted in a different stress–strain diagram. The dotted line in Fig. 19(b) was extracted from elements of a grain with 20° deviation from *Z* axis, while other grains had their previously defined misorientation. A 100 MPa difference in tensile strength was achieved by increasing the misorientation of one grain to 20°. Therefore, modeling tensile testing of a directionally solidified specimen as a simple cylinder is not accurate. Moreover, it is significant to consider the effects of both grain boundaries and misorientation in predicting tensile behavior.

5. Conclusion

Numerical simulations of a manufacturing chain from casting to mechanical behavior evaluation were conducted, and a microstructure-based model was developed for the Ni-based superalloy, GTD111. The predicted FE model of DS specimens included grain boundaries and misorientations that were generated during casting process. The FE model was verified with the experimentally manufactured DS bars. The following conclusions were obtained:

(1) It was found that nucleation parameters have a considerable effect on the grain density and the mean misorientation, although the effects of such parameters on secondary dendrite arm spacing were negligible.
(2) The results revealed that the effects of $H_{alloy/chill}$ on the thermal gradient are more pronounced in the lower two-third of the bars. In the upper one-third, the thermal gra-
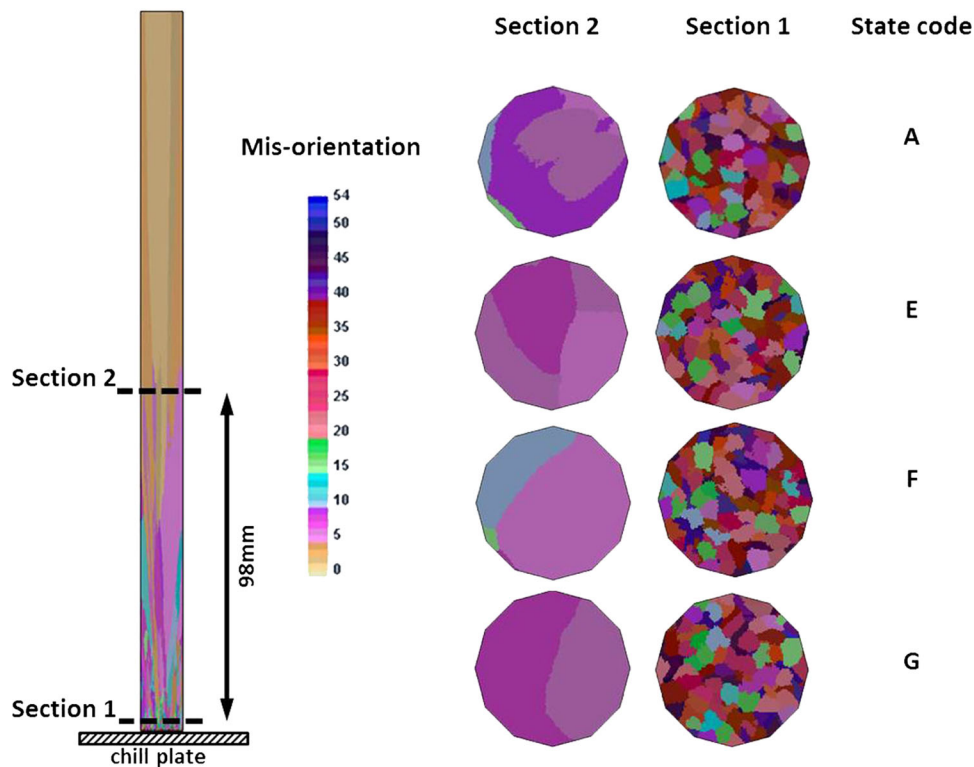
Fig. 12 Effect of heat transfer parameters on microstructure at two heights of 2 and 100 mm
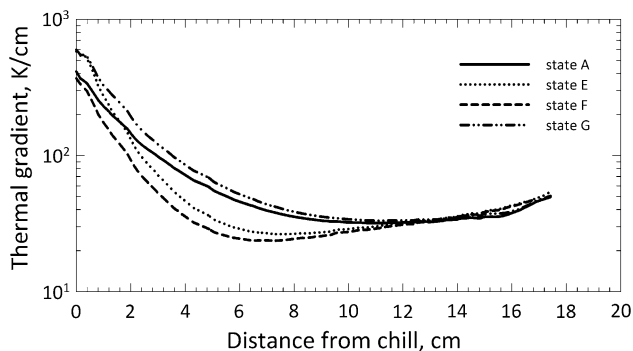

Fig. 13 Thermal gradients along the bars longitudinal axis at four different heat transfer boundary conditions
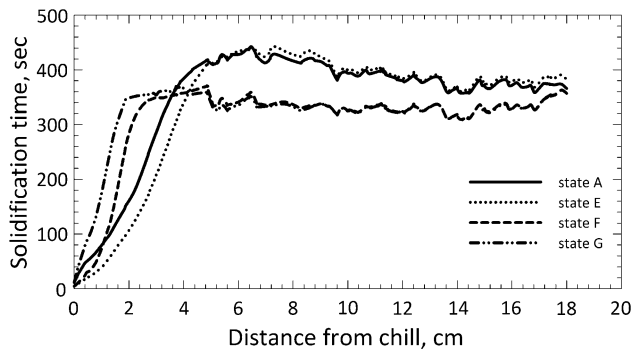

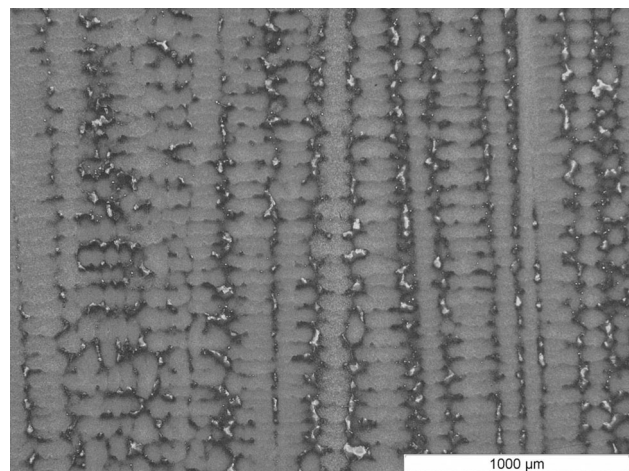**Fig. 14** Effect of alloy and shell mold heat transfer parameters on solidification time

Fig. 15 Directional growth of the dendrites in real cast bars

dient follows the same trend for different heat transfer conditions and varies between 3.0 and 4.8 K/mm.

(3) The variation of $H_{alloy/mold}$ had a considerable effect on solidification time and consequently on SDAS.

(4) SDAS was measured in the real specimens along the longitudinal axis of bars, and the scatter band of the solidification time was calculated numerically. In the power law equation describing the correlation between the SDAS and solidification time, constants were calculated as $n = 0.48$ and $17 < M < 20$.

(5) Misorientation calculated at each node through solidification modeling was applied for 3D model built-up comprising grain geometry and misorientation. The results showed the significance of considering both grain
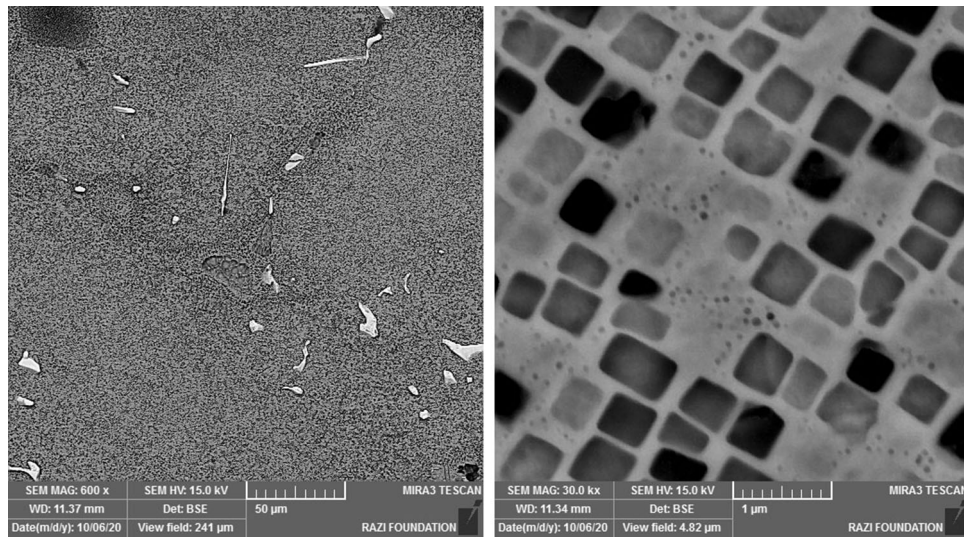
Fig. 16 Cross-sectional microstructure of a tensile specimen tested at 650 °C
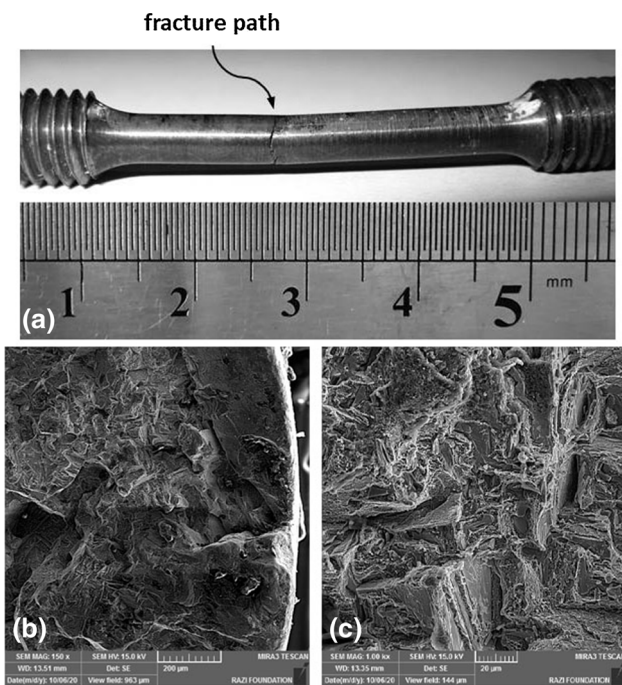

Fig. 17 Tensile specimen tested at 650 °C (a) path and location of rupture (b) and (c) FE-SEM images of edge and core of fracture surface, respectively
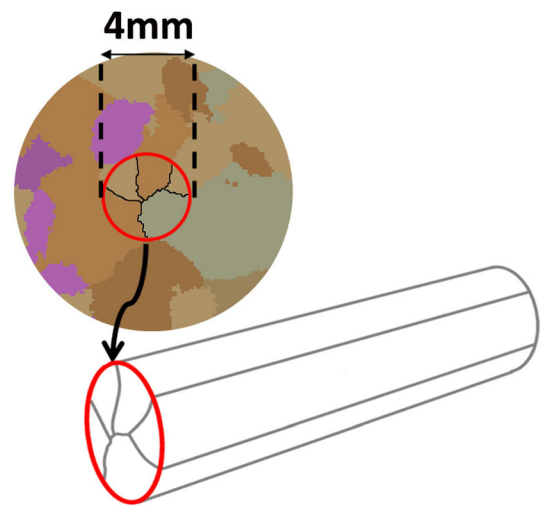

Fig. 18 Separation of a tensile specimen gauge microstructure comprising five grains, from microstructure state *C*
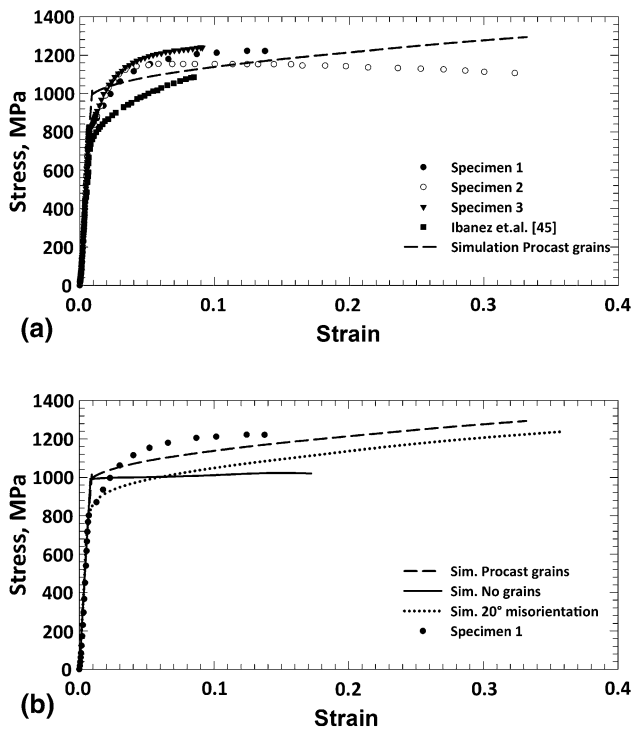
Fig. 19 Stress–strain curves for GTD111DS specimens at 650 °C in longitudinal direction: (a) experimental curves vs. state C grain structure; (b) misorientation effect in simulations

boundaries and misorientation in predicting tensile behavior.

Acknowledgments

References

1. C.M. Stewart, A.P. Gordon, E.A. Hogan, and A. Saxena, Characterization of the Creep Deformation and Rupture Behavior of DS GTD-111 Using the Kachanov–Rabotnov Constitutive Model, *J. Eng. Mater. Technol. ASME*, 2011, **133**(2), art. no. 021013

2. M. Konter, A Novel Casting Process for Single Crystal Gas Turbune Components, *Superalloys*, 2000, **2000**, p 189–200

3. C. Gandin, M. Rappaz, D. West, and B. Adams, Grain Texture Evolution during the Columnar Growth of Dendritic Alloys, *Metall. Mater. Trans. A*, 1995, **26**, p 1543–1551

4. G. Higginbotham, From Research to Cost-Effective Directional Solidification and Single-Crystal Production—An Integrated Approach, *Mater. Sci. Technol.*, 1986, **2**, p 442–460

5. A.R. Ibanez, A. Saxena, and J. Kang, Creep Behavior of a Directionally Solidified Nickel Based Superalloy, *Strength Fract. Complex.*, 2006, **4**, p 75–81

6. R.A. MacKay and R.D. Maier, The Influence Of Orientation on the Stress Rupture Properties of Nickel-Base Superalloy Single Crystals, *Metall. Trans. A*, 1982, **13**, p 1747–1754

7. D. Woodford and D. Stiles, High-Temperature Performance Evaluation of Adirectionally Solidified Nickel-Base Superalloy, *J. Mater. Eng. Perform.*, 1997, **6**, p 521–533

8. X. Yan, X. Chen, R. Sun, Y. Deng, L. Lin, and J. Nie, Investigation on Material's Fatigue Property Variation Among Different Regions of Directional Solidification Turbine Blades—Part I: Fatigue Tests on Full Scale Blades, *J. Eng. Gas Turbine Power*, 2014, **136**(10), art. no. 102502

9. R. Schafrik, S. Walston, and R. Reed, *Superalloys 2008*, TMS Publications, Warrendale, 2008

10. A. Kermanpur, N. Varahraam, E. Engilehei, M. Mohammadzadeh, and P. Davami, Directional Solidification of Ni Base Superalloy IN738LC to Improve Creep Properties, *Mater. Sci. Technol.*, 2000, **16**, p 579–586

11. A. Elliott and T. Pollock, Thermal Analysis of the Bridgman and Liquid–Metal-Cooled Directional Solidification Investment Casting Processes, *Metall. Mater. Trans. A*, 2007, **38**, p 871–882

12. S.A. Sajjadi and S. Nategh, A High Temperature Deformation Mechanism Map for the High Performance Ni-Base Superalloy GTD-111, *Mater. Sci. Eng. A*, 2001, **307**, p 158–164

13. Y. Jin, N. Bozzolo, A.D. Rollett, and M. Bernacki, 2D Finite Element Modeling of Misorientation Dependent Anisotropic Grain Growth in Polycrystalline Materials: Level Set Versus Multi-phase-Field Method, *Comput. Mater. Sci.*, 2015, **104**, p 108–123

14. S. Seo, I. Kim, C. Jo, and K. Ogi, Grain Structure Prediction of Ni-Base Superalloy Castings Using the Cellular Automaton-Finite Element Method, *Mater. Sci. Eng. A*, 2007, **449**, p 713–716

15. P. Carter, D. Cox, C. Gandin, and R.C. Reed, Process Modelling of Grain Selection during the Solidification of Single Crystal Superalloy Castings, *Mater. Sci. Eng. A*, 2000, **280**, p 233–246

16. S. Nakhodchi, D. Smith, and B. Thomas, Thermo-mechanical Behaviour during Encapsulation of Glass in a Steel Vessel, *Int. J. Press. Vessels Pip.*, 2016, **146**, p 203–215

17. C. Gandin and M. Rappaz, A 3D Cellular Automaton Algorithm for the Prediction of Dendritic Grain Growth, *Acta Mater.*, 1997, **45**, p 2187–2195

18. X. Qingyan, L. Baicheng, P. Dong, and Y. Jing, Progress on Modeling and Simulation of Directional Solidification of Superalloy Turbine Blade Casting, *China Foundry*, 2012, **9**(1), p 69–77

19. C. Gandin, J. Desbiolles, M. Rappaz, and P. Thevoz, A Three-Dimensional Cellular Automation-Finite Element Model for the Prediction of Solidification Grain Structures, *Metall. Mater. Trans. A*, 1999, **30**, p 3153–3165

20. D. Szeliga, K. Kubiak, A. Burbelko, M. Motyka, and J. Sieniawski, Modeling of Directional Solidification of Columnar Grain Structure in CMSX-4 Nickel-Based Superalloy Castings, *J. Mater. Eng. Perform.*, 2014, **23**, p 1088–1095

21. A. Kermanpur, M. Rappaz, N. Varahram, and P. Davami, Thermal and Grain-Structure Simulation in a Land-Based Turbine Blade Directionally Solidified with the Liquid Metal Cooling Process, *Metall. Mater. Trans. B*, 2000, **31**, p 1293–1304

22. M. Franke, R. Hilbinger, C. Konrad, U. Glatzel, and R. Singer, Numerical Determination of Secondary Dendrite Arm Spacing for IN738LC Investment Castings, *Metall. Mater. Trans. A*, 2011, **42**, p 1847–1853

23. G. Matache, D. Stefanescu, C. Puscasu, and E. Alexandrescu, Dendritic Segregation and Arm Spacing in Directionally Solidified CMSX-4 Superalloy, *Int. J. Cast Met. Res.*, 2016, **29**, p 303–316

24. M. Yaguchi, Anisotropic Viscoplasticity Constitutive Model for Directionally Solidified Superalloy, *Mater. High Temp.*, 2012, **29**, p 308–314

25. S.A. Sajjadi, S. Nategh, and R.I. Guthrie, Study of Microstructure and Mechanical Properties of High Performance Ni-Base Superalloy GTD-111, *Mater. Sci. Eng. A*, 2002, **325**, p 484–489

26. C. Yang, Y. Xu, Z. Zhang, H. Nie, X. Xiao, G. Jia, and Z. Shen, Improvement of Stress-Rupture Life of GTD-111 by Second Solution Heat Treatment, *Mater. Des.*, 2013, **45**, p 308–315

27. ASTM E8-04, *Standard Test Methods for Tension Testing of Metallic Materials*, ASTM International, West Conshohocken, PA, 2004

28. M. Rappaz and C.-A. Gandin, Probabilistic Modelling of Microstructure Formation in Solidification Processes, *Acta Metall. Mater.*, 1993, **41**, p 345–360

29. V. Kavoosi, S.M. Abbasi, S.G. Mirsaed, and M. Mostafaei, Influence of Cooling Rate on the Solidification Behavior and Microstructure of IN738LC Superalloy, *J. Alloys Compd.*, 2016, **680**, p 291–300

30. P. Kelly, *Solid Mechanics, Part II, Lecture Notes*, The University of Auckland, Auckland, 2013

31. M. Shenoy, D. McDowell, and R. Neu, Transversely Isotropic Viscoplasticity Model for a Directionally Solidified Ni-Base Superalloy, *Int. J. Plast.*, 2006, **22**, p 2301–2326

32. C.M. Stewart, E.A. Hogan, and A.P. Gordon, Modeling the Temperature-Dependence of Tertiary Creep Damage of a Directionally Solidified Ni-Base Superalloy, in *IMECE, ASME 2009*, p 17–25

33. T. Hyde, I. Jones, S. Peravali, W. Sun, J. Wang, and S. Leen, Anisotropic Creep Behaviour of Bridgman Notch Specimens, *Proc. Inst. Mech. Eng. Part L J. Mater. Des. Appl.*, 2005, **219**, p 163–175. https://doi.org/10.1243/146442005X10364

34. A. Rosenberg and W. Tiller, The Relationship Between Growth Forms and the Preferred Direction of Growth, *Acta Metall.*, 1957, **5**, p 565–573

35. B. Chmiela and M. Sozańska, Analysis of High Angle Boundaries in Directionally Solidified Turbine Blade Made of CMSX-4® Superalloy, in *IOP Conference Series: Materials Science and Engineering*, vol. 22, IOP Publishing, 2011

36. N.A. El-Mahallawy and M.M. Farag, Effect of Some Thermal Parameters on the Directional Solidification Process, *J. Cryst. Growth*, 1978, **44**, p 251–258

37. L. Qin, J. Shen, G. Yang, Q. Li, and Z. Shang, A Design of Non-uniform Thickness Mould for Controlling Temperature Gradient and S/L Interface Shape in Directionally Solidified Superalloy Blade, *Mater. Des.*, 2017, **116**, p 565–576

38. M. Torfeh, J. Aghazadeh, and S. Nakhodchi, Evolution of Temperature, Microstructure and Inter-granular Stresses during Directionally Solidification Process of a Ni-Based Superalloy, in *Proceedings of ASME Pressure Vessels Piping Conference*, vol. 3B, American Society of Mechanical Engineers, 2018

39. F. Yang, J. Wang, J. Yu, Z. Zhou, B. Wang, T. Tu, X. Ren, K. Deng, and Z. Ren, Microstructure and Mechanical Properties of Ni-Based Superalloy K418 Produced by the Continuous Unidirectional Solidification Process, *J. Mater. Eng. Perform.*, 2019, **28**, p 6483–6491

40. M. Rappaz, Modelling of Microstructure Formation in Solidification Processes, *Int. Mater. Rev.*, 1989, **34**, p 93–124

41. T. Haxhimali, A. Karma, F. Gonzales, and M. Rappaz, Orientation Selection in Dendritic Evolution, *Nature Mater.*, 2006, **5**, p 660–664

42. M. Ardakani, N. D'Souza, A. Wagner, B. Shollock, and M. McLean, *Competitive Grain Growth and Texture Evolution during Directional Solidification of Superalloys*, TMS Superalloys, Warrendale, 2000, p 219–228

43. C. Konrad, M. Brunner, K. Kyrgyzbaev, R. Völkl, and U. Glatzel, Determination of Heat Transfer Coefficient and Ceramic Mold Material Parameters for Alloy IN738LC Investment Castings, *J. Mater. Process. Technol.*, 2011, **211**, p 181–186

44. V. Bazhenov, A. Koltygin, Y.V. Tselovalnik, and A. Sannikov, Determination of Interface Heat Transfer Coefficient Between Aluminum Casting and Graphite Mold, *Russ. J. Non-Ferr. Met.*, 2017, **58**, p 114–123

45. W. Griffiths, A Model of the Interfacial Heat-Transfer Coefficient during Unidirectional Solidification of an Aluminum Alloy, *Metall. Mater. Trans. B*, 2000, **31**, p 285–295

46. Y. Ma, K. Yoon, and A. Saxena, Creep Crack Growth Data Reduction of Directionally Solidified Ni Base Superalloy Using C_t Estimation Scheme for Anisotropic Materials, *Mater. High Temp.*, 2015, **32**, p 289–292

47. E. Balikci, A. Raman, and R. Mirshams, Tensile Strengthening in the Nickel-Base Superalloy IN738LC, *J. Mater. Eng. Perform.*, 2000, **9**, p 324–329

48. A. Ibanez, V. Srinivasan, and A. Saxena, Creep Deformation and Rupture Behaviour of Directionally Solidified GTD 111 Superalloy, *Fatigue Fract. Eng. Mater. Struct.*, 2006, **29**, p 1010–1020

49. M.M. Shenoy, *Constitutive Modeling and Life Prediction in Ni-Base Superalloys*, Ph.D thesis, Georgia Institute of Technology, 2006

50. M.D. Trexler, *The Relationship of Microstructure to Fracture and Corrosion Behavior of a Directionally Solidified Superalloy*, Ph.D thesis, Georgia Institute of Technology, 2006

51. L.-Y. Sheng, Y. Fang, J.-T. Guo, and T.-F. Xi, Anomalous Yield and Intermediate Temperature Brittleness Behaviors of Directionally Solidified Nickel-Based Superalloy, *Trans. Nonferr. Met. Soc. China*, 2014, **24**, p 673–681

52. B. Du, Z. Hu, L. Sheng, C. Cui, J. Yang, Y. Zheng, and X. Sun, Tensile, Creep Behavior and Microstructure Evolution of an As-Cast Ni-Based K417G Polycrystalline Superalloy, *J. Mater. Sci. Technol.*, 2018, **34**, p 1805–1816